Role of hydraulic conductivity on the mechanism of earthquake induced submarine landslides – a CFD-MPM analysis

Q.A. Tran[1], E.R. Sørlie[1], G. Grimstad[1], G.R. Eiksund[1]

[1]*Department of Civil and Environmental Engineering, Norwegian University of Science and Technology, Norway*

ABSTRACT:

Submarine landslides can occur in many different soil types, for example in clay and sand. The failure mechanism and morphology of these two types of submarine landslides are quite different. Sand failures are typically characterized by sand flow slides, whereas clay failures are characterized by spread, which results from the dislocation and movement of soil blocks. There are significant differences between these types of submarine landslides due to the differences in hydraulic conductivity. It is hypothesized that the hydraulic conductivity of soil layers is a critical factor in the failure mechanism of seismic-induced submarine landslides. It is, however, unclear how the hydraulic conductivity influences the failure mechanism of seismic induced submarine landslides. Utilizing an advanced numerical technique (coupled Computational Fluid Dynamics and Material Point Method), we simulate the full process of seismic-induced submarine landslides and examine the role of the hydraulic conductivity of the soil in their failure mechanism.

Keywords: submarine landslides, Computational Fluid Dynamics, Material Point Method.

1 INTRODUCTION

Submarine landslides are a major concern in areas of high seismic activity, as they can cause considerable damage to coastal infrastructure and lead to tsunamis. Simulating the full process of a submarine landslide is difficult. This is because sediments behave as solid materials when the slide is triggered and as fluid materials when the sliding is ongoing. In recent studies, advanced numerical methods have been utilized to simulate submarine landslides, including the Material Point Method (MPM) (Shi et al., 2020), Smooth Particle Hydro Dynamics (Capone et al., 2010), Particle Finite Element Method (Zhang et al., 2019), or Coupled Eulerian Lagrangian method (Dey et al., 2016b). However, only total stress analyses (i.e., soil as a one phase material) is so far considered. As a result, we have yet to be able to quantify the role of hydraulic conductivity in the mechanism of earthquake-induced submarine landslides. Even though the hydraulic conductivity is a key factor that influences the failure mechanism of submarine landslides because it governs the change in pore water pressure (effective stress level) in the sediment.

To investigate the role of hydraulic conductivity in the failure mechanism of seismic-induced submarine landslides, we adopt the current state-of-the-art numerical technique coupled CFD-MPM model (Tran et al., 2022). In a coupled CFD-MPM method, MPM is used to deal with large deformations in solids or porous media, while CFD is used to analyze fluid dynamics. The MPM model is used for modeling the seabed and debris flows, while the CFD model is used for modeling fluid dynamics (water and air). This method preserves the advantages of both CFD and MPM by combining them together. In MPM we can define more sophisticated solid/soil constitutive models, which are essential for the initiation mechanism of the flow. Through contact laws, such as Coulomb's friction, solids (MPM materials) interact. In a contrast, CFD is the most commonly used method for simulating complex viscous fluid flows involving turbulence (fluctuations in flow) or hydroplaning (debris flows losing friction with the seabed). CFD can avoid numerical water pressure instability in modelling the fluid flow using MPM which requires additional numerical treatments such as B-bar method (Bandara & Soga, 2015) , null-space filter (Tran & Sołowski, 2019b), or least square approximation (Tran, Berzins, et al., 2019; Tran, Wobbes, et al., 2019; Zheng et al., 2021). Overall, a CFD-MPM model is able to capture the complex mechanisms of earthquake induced submarine landslides involving solid-fluid interactions.

2 PROBLEM DEFINITION

This study considers the base case shown in Figure 1. A 20-meter-high slope with a 45-degree face is placed within a horizontal and vertical structure (plane box). This structure was used as a shaking table to apply earthquake loading. To simplify earthquake loading, we simulated ground shaking for 20 seconds at a peak ground acceleration of 1g and a frequency of 2Hz (Figure 2). Ground motion is expressed in terms of velocity.

A magnitude 6 or greater earthquake can produce a similar frequency and peak ground acceleration. To highlight the role of hydraulic conductivity on the failure mechanism of earthquake-induced submarine landslides, two simulations are analysed: (1) A low hydraulic conductivity case, to mimic clay behaviour and (2) a high hydraulic conductivity case to mimic the sand behaviour. The hydraulic conductivity is calculated based on the size of the soil grain, the viscosity of the fluid, and the porosity.
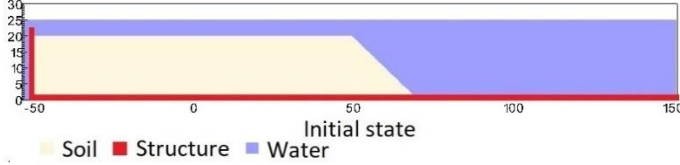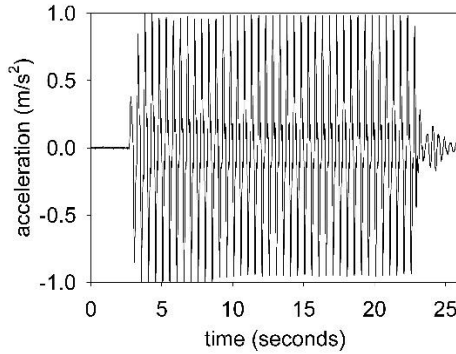

Figure 1. Geometry of the base case slope

Figure 2. Ground acceleration profile, frequency of 2Hz and magnitude of 1g

3 COUPLED CFD-MPM ANALYSIS
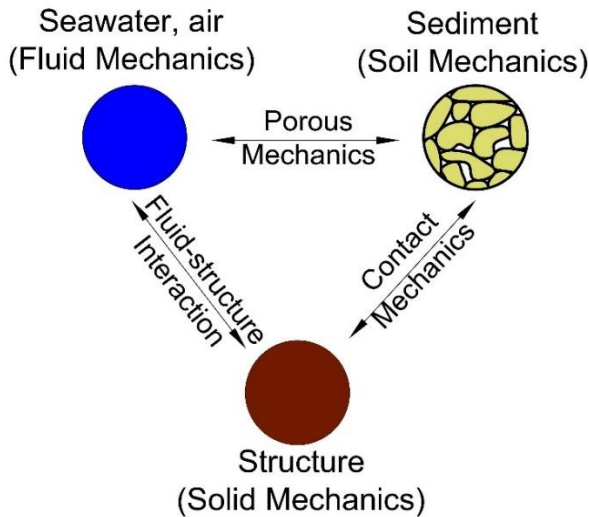
3.1 Soil-Water-Structure interaction

Figure 3. Schematic of soil-water-structure interaction

We implemented and validated the coupled CFD-MPM model in the Uintah computational framework (Tran et al., 2022) to capture the triple interaction between soil-water-structure. The CFD approach is derived from the implicit continuous-fluid Eulerian method (ICE). In ICE, all state variables are located at the cell/body centers. The state variables at cell centers are given in the

vector form of the material $r\left(M_r, \mathbf{u}_r, e_r, T_r, p, \phi_r, v_r\right)$ including mass, velocity, internal energy, temperature, pressure, volume fraction and specific volume. The MPM approach adopted the generalized interpolation technique from Bardenhagen and Kober (Bardenhagen & Kober, 2004). This method was validated with laboratory experiments (Tran et al., 2017a; Tran et al., 2017b) and large-scale landslide (Tran & Sołowski, 2019a). To couple MPM with ICE, the state variables of MPM material points including mass, velocity, temperature, and effective stress $\left(M_p, \mathbf{u}_p, T_p, \boldsymbol{\sigma}'\right)$ are mapped to cell centers using generalized interpolation technique. Then, the following governing equations are solved at the Eulerian background mesh:

Mass Balance Equation

$$\frac{1}{V}\frac{D_r M_r}{Dt} = 0 \tag{1}$$

Momentum Balance Equation for fluid

$$\frac{1}{V}\frac{D_f(M_f \mathbf{u}_f)}{Dt} = -\phi_f \nabla p + \bar{\rho}_f \mathbf{g} + \sum \mathbf{f}_d \tag{2}$$

Momentum Balance Equation for solid

$$\frac{1}{V}\frac{D_s(M_s \mathbf{u}_s)}{Dt} = \nabla \cdot \boldsymbol{\sigma}' - \phi_s \nabla p + \bar{\rho}_s \mathbf{g} - \sum \mathbf{f}_d \tag{3}$$

The last term is the momentum exchange between materials with dragging force $\mathbf{f}_d$. Apart from mass and momentum balance equations, coupled CFD-MPM also solves the energy balance equations (not presented here in), all implicitly. However, we set the numerical simulations in the isothermal condition (no thermal expansion and conduction effect) for the sake of simplicity. This is also combined with the generalized Poisson's equation to compute the fluid pressure for compressible fluid materials.

3.2 Momentum Exchange

For the momentum exchange between fluid flows and porous media, we assume that the drag force $\mathbf{f}_d$ (Beetstra et al., 2007) is given by:

$$\mathbf{f}_d = \frac{18\phi_s(1-\phi_s)\mu_f}{D_p^2} F(\phi_s, Re)(\mathbf{u}_s - \mathbf{u}_f) \tag{4}$$

where D_p is the average grain size of the grains, the solid volume fraction is ϕ_s, the fluid viscosity is μ_f, Re is the Reynolds number and the relative velocities of soil grains and fluid is $(\mathbf{u}_s - \mathbf{u}_f)$ which is calculated as:

$$Re = \frac{(1-\phi_s)\rho_f D_p}{\mu_f}\|\mathbf{u}_s - \mathbf{u}_f\| \tag{5}$$

The function $F(\phi_s, Re)$ is given as:

$$F(\phi_s, Re) = F(\phi_s, 0) + \frac{0.413Re}{24(1-\phi_s)^2} \frac{(1-\phi_s)^{-1} + 3\phi_s(1-\phi_s) + 8.4Re^{-0.343}}{1 + 10^{3\phi_s} Re^{-(1+4\phi_s)/2}} \qquad (6)$$

where the low Reynold coefficient $F(\phi_s, 0)$ is:

$$F(\phi_s, 0) = \frac{10}{(1-\phi_s)^2} + (1-\phi_s)^2(1 + 1.5\sqrt{\phi_s}) \quad (7)$$

Two grain sizes are selected for the numerical analysis (1) D_p = 0.5 mm and (2) D_p = 1e⁻⁴ mm to mimic the hydraulic conductivity of sand and clay.

3.3 Soil Models

A non-associated Mohr-Coulomb model is used for the soil. Because the Young's modulus has negligible effect on the simulations (in which plastic deformation is dominant) based on sensitivity analysis, the Young's modulus is set to be 10 kPa and Poisson's ratio is 0.3 with zero cohesion. The mobilized friction angle Φ_m' is governed following the softening curve (Figure 4) with the peak friction angle Φ_p' of 45 degrees and the residual friction angle Φ_r' of 10 degrees. The mobilized dilatancy angle is calculated from the Rowe-stress dilatancy as follow:

$$\sin \Psi_m' = \frac{\sin \Phi_m' - \sin \Phi_r'}{1 - \sin \Phi_r' \sin \Phi_m'} \qquad (8)$$
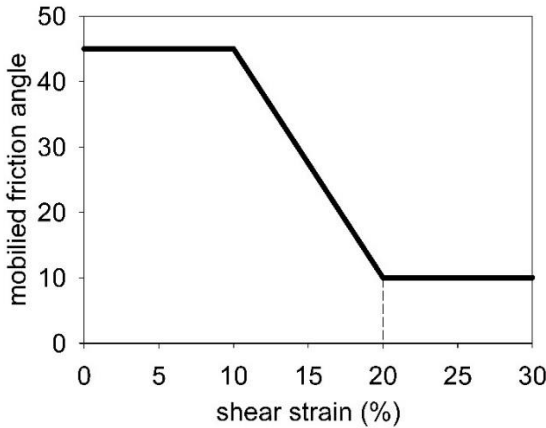

Figure 4. Mobilized friction angle in Mohr Coulomb

The contact between horizontal plane and the soil is the frictional contact with a friction coefficient of 0.1. No artificial damping is applied in the simulation. The contact between vertical plane and the sand is considered as smooth.

3.4 Fluid equation of state models

The equation of state establishes relations between thermodynamics variables. For the air, the equation of state for the perfect gas is adopted while for the water, a simple linear equation of state can be written as:

$$P_f = P_{ref} + K_f(\rho_f - \rho_{ref} - \alpha_f(T_f - T_{ref})) \quad (9)$$

where reference pressure P_{ref} = 1 atm = 101325 Pa, reference temperature T_{ref} = 10 °C, reference density ρ_{ref} = 9.998 kN/m³, the bulk modulus of water K_f = 2 GPa, and the water thermal expansion α_f = 0.18 °C⁻¹. This equation matches well with the state of the water. Under gravity, the density of the water at the water surface is 9.998 kN/m³ at the pressure of 1 atm and at the temperature of 10 °C. At the top boundary, the air has a density of 1.17 kg/m³ at the atmospheric pressure of 1 atm. At 10 Celsius degrees, air and water have viscosity of 18.45e⁻³ mPa s and 1 mPa s respectively. On all boundary faces, the symmetric boundary condition is imposed, while the Neuman boundary condition is imposed at the top boundary for pressure (dp/dx = 0 kPa) and density (dρ/dx = 0 kg/m³). The mesh size is 0.25 x 025m with 300852 element cells and 142316 material points. We consider constant temperature in the entire domain (isothermal condition) and we do not calculate the thermal expansion and thermal conduction in the numerical simulations.

4 NUMERICAL RESULTS

We compare simulations with the same input parameters except for the grain size D_p. For both cases, we demonstrate the entire process and the mechanism of earthquake-induced submarine landslides and discuss to the differences in the mechanisms.

The initial stress condition is generated by running the simulations for 10 seconds with every high hydraulic conductivity (D_p= 1m). The slope is fully consolidated after 10s under the gravity to create the initial effective stress and initial pore water pressure (see Figure 6a).

4.1 High hydraulic conductivity case (sand)

As a result of the high hydraulic conductivity, the slope collapsed right after the initial seismic event, and the failure mechanism is classified according to the updated Varnes classification as a sand flow slide (Hungr et al., 2014). The slope inclination after the landslide is less than 10 degrees (around 8 degrees see Figure 5c), which is equivalent to the residual friction angle of the soil after the landslide. It is important to note that the shear band keeps developing rapidly during the shaking and slowly after the shaking is over. There is a possibility that this is due to the secondary effect caused by the waves and turbulent flows.
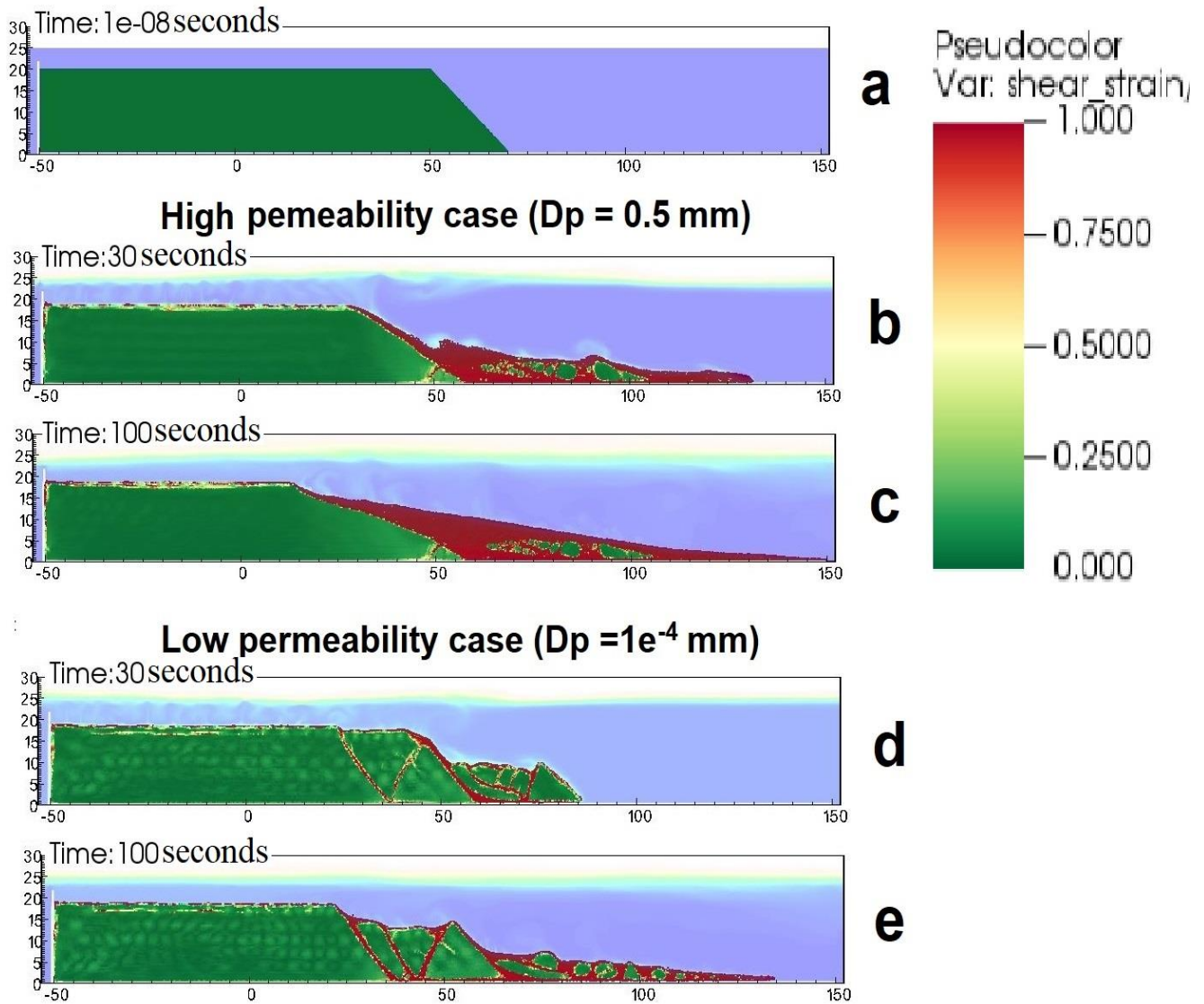
Figure 5. Shear strain development for high permeability and low permeability cases

The final inclination of the shear band is around 20 degrees (see Figure 5c). It is estimated that the wave generated by the slide is around 2-3 m high. In the event of landslides, the excess water pressure slightly changes during shaking (Figure 6b). However, this pressure quickly returns to hydrostatic pressure due to the high hydraulic conductivity of the soil during landslides. (Figure 6c).

4.2 Low permeability case (clay)

For the case of low hydraulic conductivity, the first shear band developed right after the initial event of the seismic event. The failure mechanism in this case is characterized as spread according to the updated Varnes classification (Hungr et al., 2014). The mechanism involves the formation and dislocation of undisturbed soil blocks with inclined shear bands. Based on the simulation, the slide-scare morphology of the submarine clay slide resembles the seabed morphology of the Storegga slide, which is known to be the world's largest known submarine landslide (see Figure 8).

In addition, we demonstrate the advantages of using the effective stress analysis over the total stress analysis when capturing the failure mechanism for the undrained clay slide. In the total stress analysis, one limitation is that the tip of the simulated horst was around 90 degrees (Dey et al., 2016a; Tran & Solowski, 2019), whereas, in the field, this angle was approximately 52 degrees (see Figure 7). Based on our numerical results, the tip of the simulated horst is around 65 degrees (see Figure 5e).

Unlike the high hydraulic conductivity case, negative excess water pressure increased sharply (Figure 6d) during the onset of the shear band. After the seismic event, the excess pore water pressure continues to dissipate leading to the slow run-out of the debris materials which continue to move towards the right-hand boundary (Figure 6e).
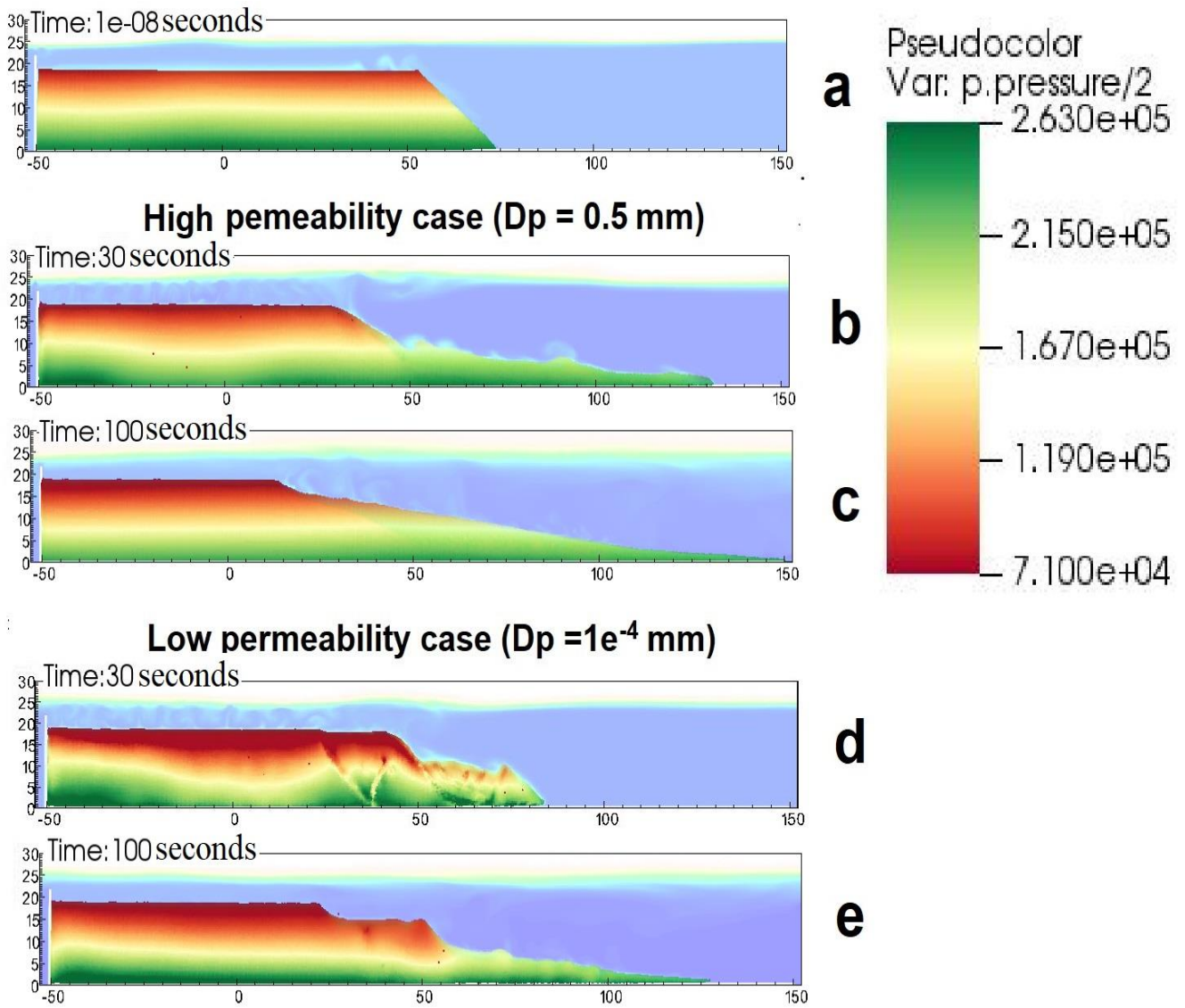
Figure 6. Pore water pressure development for high permeability and low permeability cases

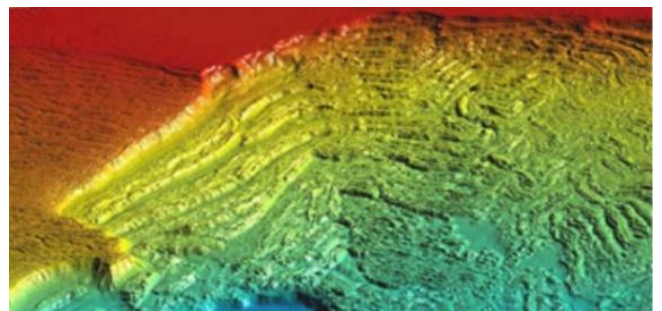Figure 7. Tip of the horst (Locat et al., 2015)

Figure 8. Seabed near the Storegga slide (Gauer et al., 2005)

5 CONCLUSIONS

We present a numerical approach that combines CFD-MPM to capture the complicated triple interaction between soil, water, and structure. We also show the completed process of earthquake induced submarine landslides including (1) earthquake triggering mechanism, (2) the onset of the shear band with the development of pore water pressure, (3) progressive failure mechanism, and (4) submarine landslide induced wave to final deposition.

The hydraulic conductivity also plays an important role in the failure mechanism of earthquake-induced submarine landslides. As a result of the high permeability of the material, the mechanism is characterized as a sand flow slide with rapid movement of the saturated debris material. When hydraulic conductivity is low, the mechanism is characterized as a spread with the dislocation and formation of soil blocks. We also capture a more realistic tip angle of the horst in comparison to the one-phase model previously presented in the literature.

This research can be used to better understand the failure mechanisms of submarine landslides and to develop better methods for predicting and mitigating their potential damage. It is necessary to conduct further research to better understand the complex relationship between hydraulic conductivity, soil properties, and the failure mechanisms of submarine landslides. This is to improve the prediction of landslide susceptibility and to improve coastal zone management.

6 ACKNOWLEDGEMENTS

7 REFERENCES

Bandara, S., & Soga, K. (2015). Coupling of soil deformation and pore fluid flow using material point method (vol 663, pg 199, 2015). *Computers and Geotechnics*, *65*, 302-302.

Bardenhagen, S. G., & Kober, E. M. (2004). The Generalized Interpolation Material Point Method. *Computer Modeling in Engineering & Sciences*, *5*(6), 477-496.

Beetstra, R., van der Hoef, M. A., & Kuipers, J. A. M. (2007). Drag force of intermediate Reynolds number flow past mono- and bidisperse arrays of spheres. *Aiche Journal*, *53*(2), 489-501.

Capone, T., Panizzo, A., & Monaghan, J. (2010). SPH modelling of water waves generated by submarine landslides. *Journal of Hydraulic Research*, *48*(1), 80-84.

Dey, R., Hawlader, B. C., Phillips, R., & Soga, K. (2016a). Numerical modelling of submarine landslides with sensitive clay layers. *Geotechnique*, *66*(6), 454-468.

Dey, R., Hawlader, C., Phillips, R., & Soga, K. (2016b). Numerical modelling of submarine landslides with sensitive clay layers. *Géotechnique*, *66*(6), 454-468.

Gauer, P., Kvalstad, T. J., Forsberg, C. F., Bryn, P., & Berg, K. (2005). The last phase of the Storegga Slide: simulation of retrogressive slide dynamics and comparison with slide-scar morphology. *Marine and Petroleum Geology*, *22*(1-2), 171-178.

Hungr, O., Leroueil, S., & Picarelli, L. (2014). The Varnes classification of landslide types, an update. *Landslides*, *11*(2), 167-194.

Locat, A., Leroueil, S., Fortin, A., Demers, D., & Jostad, H. P. (2015). The 1994 landslide at Sainte-Monique, Quebec: geotechnical investigation and application of progressive failure analysis. *Canadian Geotechnical Journal*, *52*(4), 490-504.

Shi, J. J., Zhang, W., Wang, B., Li, C. Y., & Pan, B. (2020). Simulation of a Submarine Landslide Using the Coupled Material Point Method. *Mathematical Problems in Engineering*, *2020*.

Tran, Q. A., Berzins, M., & Sołowski, W. (2019). An improved moving least squares method for the Material Point Method. International Conference on the Material Point Method for Modelling Soil-Water-Structure Interaction, Cambridge, UK.

Tran, Q. A., Grimstad, G., & Ghoreishian Amiri, S. A. (2022). MPMICE: A hybrid MPM-CFD model for simulating coupled problems in porous media. Application to earthquake-induced submarine landslides. *arXiv preprint*.

Tran, Q. A., & Solowski, W. (2019). Generalized Interpolation Material Point Method modelling of large deformation problems including strain-rate effects - Application to penetration and progressive failure problems. *Computers and Geotechnics*, *106*, 249-265.

Tran, Q. A., & Sołowski, W. (2019a). Generalized Interpolation Material Point Method modelling of large deformation problems including strain-rate effects – Application to penetration and progressive failure problems. *Computers and Geotechnics*, *106*, 249-265.

Tran, Q. A., & Sołowski, W. (2019b). Temporal and null-space filter for the material point method. *International Journal for Numerical Methods in Engineering*, *120*(3), 328-360.

Tran, Q. A., Solowski, W., Karstunen, M., & Korkiala-Tanttu, L. (2017a). Modelling of fall-cone tests with strain-rate effects. *Proceedings of the 1st International Conference on the Material Point Method (Mpm 2017)*, *175*, 293-301.

Tran, Q. A., Solowski, W., Thakur, V., & Karstunen, M. (2017b). Modelling of the Quickness Test of Sensitive Clays Using the Generalized Interpolation Material Point Method. Landslides in Sensitive Clays. Advances in Natural and Technological Hazards Research,

Tran, Q. A., Wobbes, E. D., Sołowski, W., Moller, M., & Vuik, C. (2019). Moving least squares reconstruction for B-spline Material Point Method. International Conference on the Material Point Method for Modelling Soil-Water-Structure Interaction, Cambridge, UK.

Zhang, X., Onate, E., Torres, S. A. G., Bleyer, J., & Krabbenhoft, K. (2019). A unified Lagrangian formulation for solid and fluid dynamics and its possibility for modelling submarine landslides and their consequences. *Computer methods in applied mechanics and engineering*, *343*, 314-338.

Zheng, X., Pisano, F., Vardon, P., & Hicks, M. A. (2021). An explicit stabilised material point method for coupled hydromechanical problems in two-phase porous media. *Computers and Geotechnics*, *135*, 104112.